INTERNATIONAL JOURNAL FOR NUMERICAL METHODS IN FLUIDS
Int. J. Numer. Meth. Fluids 2004; **46**:315–344 (DOI: 10.1002/fld.755)

Numerical study of physiological turbulent flows through series arterial stenoses

T. S. Lee*,†, Wei Liao and H. T. Low

Mechanical Engineering Department, National University of Singapore, Singapore 119260, Singapore

SUMMARY

A numerical investigation on the characteristics of transitional turbulent flow over series bell-shape stenoses for a physiological pulsatile flow is presented in the present study. The flow behaviours for the physiological pulsatile flow are studied by considering the effects of the Reynolds number, Womersley number, constriction ratio and spacing ratio of the stenoses on the pulsatile turbulent flow fields. Especially, the mutual influences between the double stenoses under different flow conditions are considered. The numerical results show that the variation of these flow parameters puts significant impacts on the flow developments in the arteries with series stenoses. The double stenoses lead to the higher peak turbulence disturbance and the greater area with comparatively high turbulence intensity distal to the stenoses in comparison with the single stenosis. The analysis shows that for the physiological pulsatile flow, the downstream stenosis usually does not have perceptible influences on the upstream flow fields.

KEY WORDS: series stenoses; physiological pulsatile; turbulence; numerical simulation

1. INTRODUCTION

The occurrence of turbulence in the arteries has long been realized [1]. The blood flow through arteries is inherently unsteady due to the cyclic nature of the heart pump and the Reynolds number can vary from $O(1)$ in the small arterioles to as high as $O(10^3)$ in the larger arteries. Although it is firmly established that steady laminar flow through a pipe becomes unstable at a Reynolds number (based on the mean velocity and pipe diameter) of about 2300, the possibility of generating turbulence is greatly increased by the occurrence of stenosis in the artery. The obstruction presented by moderate and severe stenosis can lead to a highly disturbed flow region at the downstream of the stenosis. These disturbed flows may either remain laminar or undergo transition to turbulent flow, depending upon the specific flow conditions through the stenosis and the geometry of the stenosis.

*Correspondence to: T. S. Lee, Mechanical Engineering Department, National University of Singapore, Singapore 119260, Singapore.
†E-mail: mpeleets@nus.edu.sg

Published online 14 July 2004
Received 5 May 2003
Revised 15 November 2004

Turbulence represents an abnormal flow condition in the circulation and the development of turbulent flow in arteries has important clinical consequences. Ku [2] pointed out that for high-grade stenoses, turbulence is the major loss mechanism. Turbulence can have a dramatic influence on the pressure drop and wall shear stresses in the post-stenotic region, both of which can have a substantial negative influence on the cardiovascular system. At the same time, better understanding of flow and turbulence in post-stenotic flow could possibly lead to more accurate diagnostic procedures for locating severe stenosis in the future [3]. Actually, numerous experimental studies for steady turbulent flow in arteries have been carried out by many researchers, such as Clark [4], Deshpande and Giddens [5] and Ahmed and Giddens [6]. These studies have shown that, even with relatively mild stenosis, transitional flow or turbulence can be expected distal to the stenosis. The unsteady turbulence experiments are very difficult to implement and only a few fundamental experimental studies can be found for the pulsatile turbulent flow through stenosis. Yongchareon [7] researched the relationship between the critical Reynolds number and some dimensionless frequency parameters and between the critical Reynolds number and the shape of the constrictions, respectively. Ahmed [8] measured the flow disturbances in the downstream region of modelled stenosis with pulsatile inlet flow for mean Reynolds number 600. The experiments presented are far from sufficient for recognizing the nature of unsteady turbulent flow in arteries.

Numerical simulation of blood flow offers a non-invasive means of obtaining detailed flow patterns, such as wall shear stress distributions, which are very difficult to obtain experimentally. Most numerical simulations of turbulent flows through the stenosis were limited to steady flows, such as those by Deshpande [9] and Ghalichi *et al.* [10]. The numerical simulation on the pulsatile turbulent flow is full of challenges. The occurrence of turbulence makes the process of numerical simulation much more complicated and difficult. So far, there are very few works on the pulsatile turbulent flow in the tube with stenosis. Mittal *et al.* [3] applied the Large-eddy simulation to study the pulsatile turbulent flow in a planar channel with a one-sided semicircular stenosis. The planar geometric model is not realistic and does not account for the actual circular arterial lumen. Liao *et al.* [11] compared the three different types of pulsatile turbulent flows in the tube with a single axisymmetrical bell-shape stenosis and studied numerically the physiological pulsatile flow fields under different flow conditions.

Multiple stenoses in diseased vascular tube may occur because of the formation of the primary stenosis that can result in downstream circulation flow. The downstream circulation in time will accumulate particles and then lead to the formation of a secondary stenosis. As a result of the secondary stenosis, a circulation zone will form at its downstream, thus resulting in a third stenosis, etc. The effects of these stenoses result in a series of sequence constrictions. A study on the flow through double stenoses was initially presented by Lee [12, 13] for laminar flow. Damodaran *et al.* [14] also numerically researched the steady laminar flows through the multiple constrictions in tubes for a range of Reynolds number 50–250. Numerical solutions to the steady turbulent flows through double bell-shaped stenoses have been reported by Lee *et al.* [15] in which the steady turbulent flows in a circular tube were studied for the Reynolds number range 100–4000 with different constriction ratios and spacing ratios of stenoses. To our knowledge, no numerical investigation has studied the pulsatile turbulent flow through series arterial stenoses.

In the present study, the physiological pulsatile turbulent flows in the tube with double bell-shape stenoses are investigated in detail. The flow behaviours for physiological pulsatile flows are studied by considering the effects of the Reynolds number, Womersley number,

constriction ratio and spacing ratio of the stenoses on the pulsatile turbulent flow fields. Especially, the present work studies the mutual influences of the double stenoses in detail under different flow conditions.

The blood flow in the arteries mainly lies in the low Reynolds number range. Under this flow condition, it is often seen that the turbulent, laminar and transitional regions coexist in the stenosed flow field commonly with large separation bubble. As Wilcox [16] pointed out, therefore, the blood flow through the arterial stenosis is particularly difficult to simulate among the various separated-flow applications. In the present work, the pulsatile turbulent flow fields in stenosed arterial tubes are simulated numerically using the method which has been developed by Lee *et al.* [17, 18] for solving the steady and unsteady incompressible Navier–Stokes equations and k–ω turbulence model equations in a curvilinear co-ordinate system. The numerical solutions are obtained under the conditions of Newtonian fluid and rigid wall.

2. GOVERNING EQUATIONS AND NUMERICAL METHODS

Basing on the eddy viscosity concept and turbulence model closure, for axially symmetric flow of incompressible Newtonian fluids, the Reynolds-average governing equations of two-dimensional flow can be written in axisymmetric co-ordinate system as follows:

$$\frac{\partial(ru)}{\partial z}+\frac{\partial(rv)}{\partial r}=0 \tag{1a}$$

$$\frac{\partial(ru)}{\partial t}+\frac{\partial(ru^2)}{\partial z}+\frac{\partial(ruv)}{\partial r} =-\frac{\partial(rp)}{\partial z}+\frac{\partial}{\partial z}\left(r(\nu+\nu_t)\frac{\partial u}{\partial z}\right)+\frac{\partial}{\partial r}\left(r(\nu+\nu_t)\frac{\partial u}{\partial r}\right) \tag{1b}$$

$$\frac{\partial(rv)}{\partial t}+\frac{\partial(ruv)}{\partial z}+\frac{\partial(rv^2)}{\partial r} =-\frac{\partial(rp)}{\partial r}+\frac{\partial}{\partial z}\left(r(\nu+\nu_t)\frac{\partial v}{\partial z}\right)+\frac{\partial}{\partial r}\left(r(\nu+\nu_t)\frac{\partial v}{\partial r}\right)+p-\nu\frac{v}{r} \tag{1c}$$

Here u and v are the velocity components in z and r directions, respectively.

The governing equations of Wilcox's k–ω turbulence model [16] for unsteady-state axisymmetric turbulent flow are written as follows:

$$\frac{\partial(rk)}{\partial t}+\frac{\partial(ruk)}{\partial z}+\frac{\partial(rvk)}{\partial r} =r\nu_t P_d+\frac{\partial}{\partial z}\left[r(\nu+\sigma_k\nu_t)\frac{\partial k}{\partial z}\right]+\frac{\partial}{\partial r}\left[r(\nu+\sigma_k\nu_t)\frac{\partial k}{\partial r}\right]-r\beta_k k\omega \tag{2a}$$

$$\frac{\partial(r\omega)}{\partial t}+\frac{\partial(ru\omega)}{\partial z}+\frac{\partial(rv\omega)}{\partial r}$$
$$=r\gamma_\omega P_d+\frac{\partial}{\partial z}\left[r(\nu+\sigma_\omega\nu_t)\frac{\partial\omega}{\partial z}\right]+\frac{\partial}{\partial r}\left[r(\nu+\sigma_\omega\nu_t)\frac{\partial\omega}{\partial r}\right]-r\beta_\omega\omega^2 \tag{2b}$$

Here

$$P_d=2\left[\left(\frac{\partial u}{\partial z}\right)^2+\left(\frac{\partial v}{\partial r}\right)^2+\left(\frac{v}{r}\right)^2\right]+\left(\frac{\partial u}{\partial r}+\frac{\partial v}{\partial z}\right)^2 \tag{2c}$$

The eddy viscosity is calculated from

$$\nu_t=\frac{k}{\omega} \tag{3}$$

The closure coefficients for the Wilcox k–ω model are

$$\beta_k=0.09,\quad \sigma_k=0.5,\quad \beta_\omega=0.075,\quad \sigma_\omega=0.5,\quad \gamma_\omega=5/9$$

In Equation (2a)–(2c), k and ω represent the turbulence kinetic energy and specific dissipation rate, respectively.

As shown in References [17, 18], the artificial compressibility approach presented by Chorin [19] initially just for steady flow has been developed to solve both steady and unsteady laminar and turbulent flows. In the present study, the artificial compressibility formulation developed by Lee *et al.* [17, 18] is used to solving pulsatile turbulent flows through arterial stenosis. Basing on Boussinesq's hypothesis, therefore, the non-dimensional incompressible Reynolds-averaged Navier–Stokes equations with the modification of artificial compressibility are reformulated in a generalized curvilinear co-ordinate system with the axisymmetric physical components taken as the dependent variables:

$$\frac{\partial W}{\partial\tau}+K\frac{\partial W}{\partial t}+\frac{\partial E}{\partial\xi}+\frac{\partial F}{\partial\eta}=\frac{\partial E_V}{\partial\xi}+\frac{\partial F_V}{\partial\eta}+S \tag{4}$$

where

$$W=Jr\begin{bmatrix}p\\u\\v\end{bmatrix}$$

$$E=Jr\begin{bmatrix}\beta U\\uU+p\xi_z\\vU+p\xi_r\end{bmatrix},\quad F=Jr\begin{bmatrix}\beta V\\uV+p\eta_z\\vV+p\eta_r\end{bmatrix}$$

$$E_v = Jr\frac{1}{Re}(1+v_t)\begin{bmatrix}0\\ \alpha_1 u_\xi + \alpha_2 u_\eta\\ \alpha_1 v_\xi + \alpha_2 v_\eta\end{bmatrix}, \quad F_v = Jr\frac{1}{Re}(1+v_t)\begin{bmatrix}0\\ \alpha_2 u_\xi + \alpha_3 u_\eta\\ \alpha_2 v_\xi + \alpha_3 v_\eta\end{bmatrix}$$

$$S = Jr\begin{bmatrix}0\\ 0\\ \dfrac{p}{r} - \dfrac{1}{Re}(1+v_t)\dfrac{v}{r^2}\end{bmatrix}$$

$$K = St\begin{bmatrix}0 & 0 & 0\\ 0 & 1 & 0\\ 0 & 0 & 1\end{bmatrix} \quad \text{(for unsteady flow)}$$

$$K = 0 \quad \text{(for steady flow)}$$

In the governing equations with dual time, τ is a pseudo-time variable and t is the physical time. β is an artificial compressibility parameter and J is the Jacobian of the transformation. U, V are contravariant velocities in ξ, η-direction given by

$$U = \xi_z u + \xi_r v$$

$$V = \eta_z u + \eta_r v$$

and

$$\alpha_1 = \xi_z^2 + \xi_r^2, \quad \alpha_2 = \xi_z\eta_z + \xi_r\eta_r, \quad \alpha_3 = \eta_z^2 + \eta_r^2$$

v_t is the eddy viscosity that is calculated by the k–ω turbulence model.

Similar to the Navier–Stokes equations, the k–ω model equations are also non-dimensionalized and reformulated in a generalized curvilinear co-ordinate system taking the axisymmetric physical components as the dependent variables. It results in the following system of equations in conservation form with dual time:

$$\frac{\partial \tilde{W}}{\partial \tau} + \tilde{K}\frac{\partial \tilde{W}}{\partial t} + \frac{\partial \tilde{E}}{\partial \xi} + \frac{\partial \tilde{F}}{\partial \eta} = \frac{\partial \tilde{E}_V}{\partial \xi} + \frac{\partial \tilde{F}_V}{\partial \eta} + \tilde{S} \tag{5}$$

where

$$\tilde{W} = Jr\begin{bmatrix}k\\ \omega\end{bmatrix}$$

$$\tilde{E} = Jr\begin{bmatrix}Uk\\ U\omega\end{bmatrix}, \quad \tilde{F} = Jr\begin{bmatrix}Vk\\ V\omega\end{bmatrix}$$

$$\tilde{E}_v = Jr\,\frac{1}{Re}\begin{bmatrix}(1+\sigma_k v_t)(\alpha_1 k_\xi + \alpha_2 k_\eta)\\(1+\sigma_\omega v_t)(\alpha_1 \omega_\xi + \alpha_2 \omega_\eta)\end{bmatrix}$$

$$\tilde{F}_v = Jr\,\frac{1}{Re}\begin{bmatrix}(1+\sigma_k v_t)(\alpha_2 k_\xi + \alpha_3 k_\eta)\\(1+\sigma_\omega v_t)(\alpha_2 \omega_\xi + \alpha_3 \omega_\eta)\end{bmatrix}$$

$$\tilde{S} = Jr\begin{bmatrix}v_t P_d - \beta_k k\omega\\ \gamma_\omega P_d - \beta_\omega \omega^2\end{bmatrix}$$

$$\tilde{K} = St\begin{bmatrix}1 & 0\\0 & 1\end{bmatrix} \quad \text{(for unsteady flow)}, \quad \tilde{K} = 0 \quad \text{(for steady flow)}$$

$$P_d = 2\left[(u_\xi \xi_z + u_\eta \eta_z)^2 + (v_\xi \xi_r + v_\eta \eta_r)^2 + \left(\frac{v}{r}\right)^2\right] + (u_\xi \xi_r + u_\eta \eta_r + v_\xi \xi_z + v_\eta \eta_z)^2 \tag{6}$$

Then the eddy viscosity is obtained from

$$v_t = Re\,\frac{k}{\omega} \tag{7}$$

In Equations (4) and (5), the dimensionless variables $r^* = r/r_0$, $z^* = z/r_0$, $u^* = u/u_0$, $v^* = v/u_0$, $t^* = t/t_0$, $p^* = p/\rho u_0^2$, $k^* = k/u_0^2$ and $\omega^* = \omega r_0/u_0$ have been used and asterisks are dropped for brevity. $St = r_0/(u_0 t_0)$ and $Re = r_0 u_0/v$ are the Strouhal number and Reynolds number, respectively. Generally, t_0 is taken as $1/\varphi$ for a pulsatile flow under the assumption that φ is the angular frequency of the pulsatile flow.

In deriving the Navier–Stokes and turbulence model equations, constant density is assumed for simplicity. As has been shown above, the system of governing equations can be used to describe both steady and unsteady flow. The whole set of differential equations is physically unbalanced until the steady state solution in pseudo-time is reached. The present study is based on a reasonable assumption that the time scale of the pulsatile phenomena is much larger than the characteristic time scale of turbulence in large arteries. Actually, Wood [20] pointed out that the frequency range of the turbulent in a large artery is usually from 10^2 to 10^4 Hz while the frequency of the heart rate is about 1–2 Hz.

In the present study, the solution procedure is based on the method of artificial compressibility and uses a decoupled approach to solve the Reynolds-averaged Navier–Stokes equations and k–ω turbulence model equations. The decoupled approach is applied to improve the efficiency and flexibility of the code. In the current decoupled approach, the Reynolds-averaged Navier–Stokes equations are implicitly solved to update the pressure and the velocity field; then the k–ω model equations are solved together with the new given velocities to compute a new turbulent viscosity field. The above process is repeated until the convergence criterion is satisfied. The Lower–Upper Symmetric-Gauss–Seidel (LU-SGS) implicit algorithm is used as the time integration scheme for the governing equations because of its efficiency and stability. When constructing this scheme, the advantages of recent advances in computational fluid dynamics are taken into considerations. The LU-SGS method is applied with the use of upwind-biased and Total Variation Diminishing (TVD) scheme. To calculate the convective

flux, an edge-based method is used by calculating and storing the flux integrals based on edges. The convective fluxes are discretized by using the appropriate form of Roe's flux-difference splitting [17, 21]. The high-order upwind-biased Monotonic Upstream Schemes for Conservation Laws (MUSCL) scheme with satisfying TVD conditions is used to deal with the convective terms, which is helpful to stabilize the computation and increase the convergent speed. This is because the steep gradients exist in the k, ω fields. In a typical profile of ω normal to the wall, the value of ω can vary rapidly from $O(10^4)$ (even the value is higher for finer grids) near the wall to $O(1)$ outside the boundary layer. The high-resolution TVD scheme is just designed to deal with such large gradients. The viscous terms are evaluated by the second-order central difference. The details and validation of the current numerical method for incompressible flows can be found in References [17, 18].

The artificial compressibility parameter β influences both the stability and the efficiency in the numerical computation. However, it is easy to find a range of β for which the code can converge very quickly. As has been referred to in References [17, 18], the current method is found not to be sensitive to the value of the artificial compressibility parameter and the present code is stable for a wide range of β. In the present study, a constant value of the parameter β has been used. For all cases, the value of β is set to 100 that is found to give a good rate of convergence and accuracy for the problems considered.

3. GEOMETRY AND BOUNDARY CONDITIONS

In the present study, the geometrical configuration of the vascular tube with a stenosis and its co-ordinate system are shown in Figure 1. The co-ordinate variables (r, z) are defined in the cylinder co-ordinate system; L is the length of the tube under consideration; D is the diameter of the tube having a constant cross-section; d_c is the opening of the constriction; s_1, s_2 are distances of the first and second stenosis from inlet plane, respectively; and s is the spacing between stenoses, $s = (s_2 - s_1)$.

The geometry of the stenosis may be described by the following bell-shaped Gaussian distribution profile [12]:

$$f(z) = 1 - c_i \exp(-c_s(z - s_i)^2) \tag{8}$$

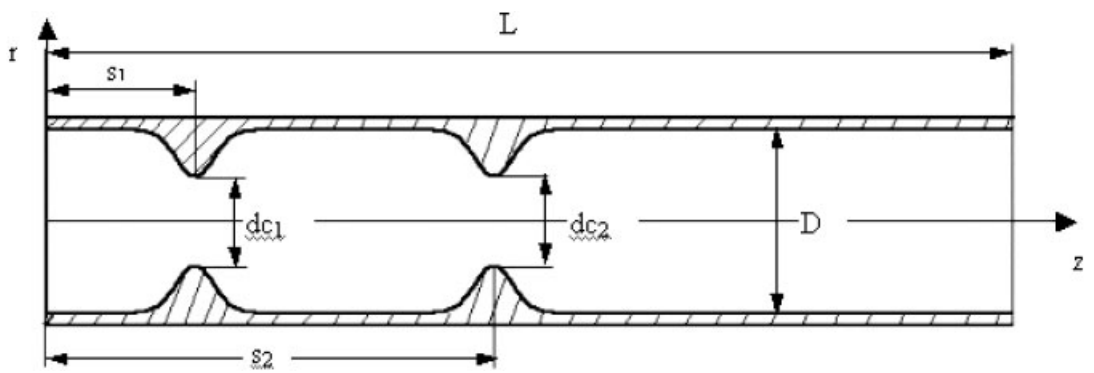

Figure 1. The geometry of the stenosis.

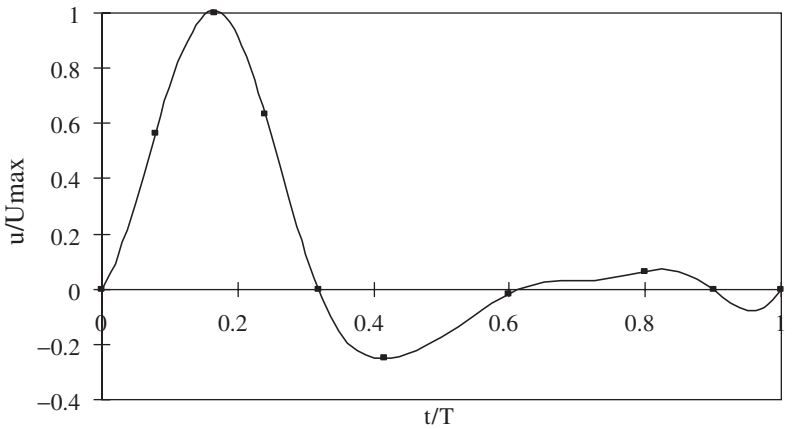

Figure 2. Time variation of the velocity for the physiological pulsatile flow, equivalent pulsatile flow and simple pulsatile flow.

where c_s is a shape constant; z_1, z_2 are limits of the first constriction and z_3, z_4 are limits of the second constriction; c_i is constriction ratio $(D-d_{ci})/D$. c_1 is the upstream stenosis constriction ratios defined as $c_1=(D-d_{c1})/D$; c_2 is the downstream stenosis constriction ratios defined as $c_2=(D-d_{c2})/D$. In this study, c_s is fixed at 1.0.

The boundary types encountered in the present study are classified as inflow, outflow, solid wall and symmetrical plane. All boundary conditions are imposed using halo cells that are two rows of fictitious cells next to the boundary. With this concept, the boundary fluxes can be treated in a fashion similar to the internal fluxes. On a solid surface, the usual non-slip condition is applied. At the outflow boundary the velocities are extrapolated from the interior and a constant static pressure is imposed. At the inflow boundary, the velocities are specified and the pressure is extrapolated from the interior. At the upstream inlet, there is not the known velocity profile to be found for different inflow conditions. Therefore, the computational domain is extended to ensure the length of $20r_0$ upstream the first stenosis and $20r_0$ downstream the second stenosis in order to eliminate the effects of inlet and outlet boundary conditions. For the pulsatile flows through arterial stenosis in the present study, the average inlet velocity is specified by a physiological pulsatile profile as shown in Figure 2. Here $u(t)$ is the same as that given by other researchers [22, 23]. The physiological flow is considered here due to its direct relevance with the investigation of intracardiac flow, blood vessel stenosis and heart valvular regurgitation.

In this work, the boundary types encountered when solving k–ω equations are also classified as inflow, outflow, solid wall and symmetrical plane. At the inflow, in nondimensional form k and ω are set at very low levels, i.e.

$$k_{\text{in}} = 1.5 I_{\text{T}}^2 u_{\text{in}}^2, \quad \omega_{\text{in}} = \frac{\sqrt{k_{\text{in}}}}{C_\mu^{1/4} l_{\text{in}}} \tag{9}$$

where I_T is the turbulence intensity, usually taken to be 1%, $C_\mu = 0.09$ and l_{in} is the length scale given by

$$l_{in} = \min(\kappa y_{wall}, 0.1R_0) \tag{10}$$

Here y_{wall} is the normal distance from the wall and $\kappa = 0.41$ denotes the universal von Karman constant. The non-slip wall boundary conditions for the k–ω model equations are

$$k = 0, \quad \omega = \frac{6\nu}{\beta_\omega y_1} \tag{11}$$

At the outflow boundary, the streamwise gradients of k and ω are assumed zero, i.e.

$$\frac{\partial k}{\partial z} = \frac{\partial \omega}{\partial z} = 0 \tag{12}$$

Along the axis of symmetry, the gradients of k and ω in r direction are assumed zero, i.e.

$$\frac{\partial k}{\partial r} = \frac{\partial \omega}{\partial r} = 0 \tag{13}$$

In the present study, the dimensionless Reynolds number, Womersley number and Strouhal number are defined as, respectively,

$$Re = \frac{u_0 r_0}{\nu}$$

$$Wo = r_0 \sqrt{\frac{\varphi}{\nu}} \tag{14}$$

$$St = \frac{Wo^2}{Re} = \frac{r_0 \varphi}{u_0}$$

where r_0 is the radius of the tube infinitely far upstream where the section becomes uniform; u_0 is the maximum value, in the period, of the average velocity over the section of inlet; φ is the angular frequency of the pulsatile flow. The Womersley number is an indication of the main frequency of the flow. In physiological situations, the frequency of the flow is determined by the heart rate.

4. VALIDATION OF NUMERICAL METHOD

In our previous study [17, 18], a variety of computed results have been presented to validate the present numerical method and computer code. Here two test cases are presented to further validate the capacity of the current methods for predicting the turbulent flows in relatively low Reynolds numbers.

4.1. Steady flow inside a tube with a constriction for $Re = 2000$

This case deals with the steady turbulent flow inside a circular tube with a constriction for a relatively low Reynolds number. This flow has been studied experimentally by Ahmed

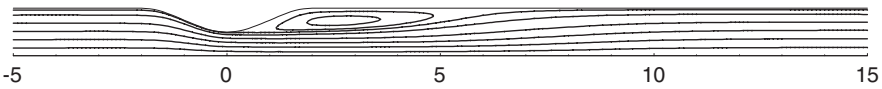

Figure 3. Streamlines for the turbulent flow through a constriction at $Re = 2000$.

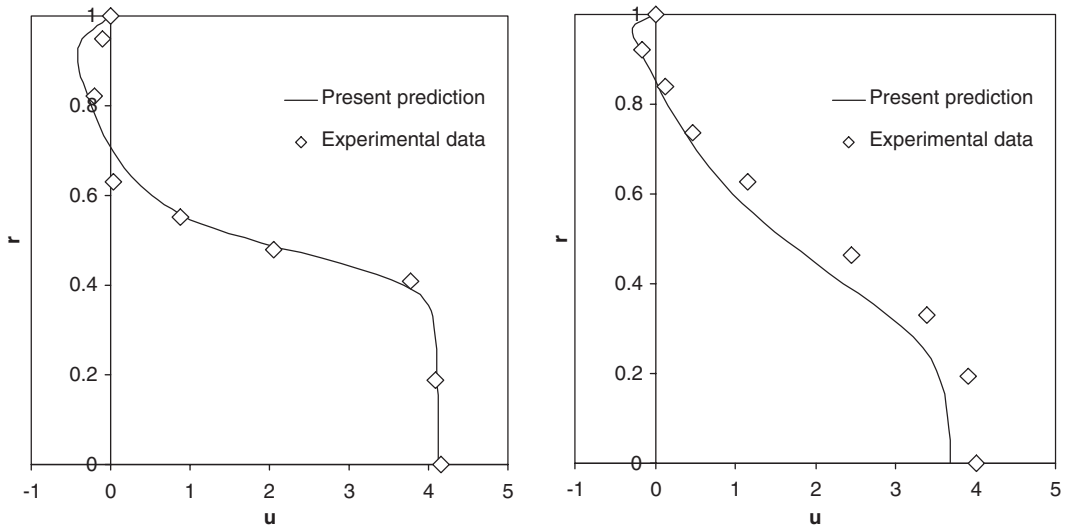

Figure 4. Comparison of computed and measured [6] axial velocity profiles at different axial positions.

et al. [6]. The geometry of the axisymmetric constriction may be described by the following profile:

$$\frac{r}{r_0} = 1 - \frac{\delta}{2r_0}\left(1 + \cos\frac{\pi z}{z_0}\right), \quad -z_0 \leqslant z \leqslant z_0 \tag{15}$$

In this case, $\delta = \frac{1}{2}r_0$, $z_0 = 2.0$.

The Reynolds number is set to 2000, which is based on the diameter and the average inlet velocity. In this case, the computational domain is extended from z-position $-15r_0$ to $18r_0$. Below presented are some results computed on a 231×33 grid, which gives sufficient resolution, as verified by mesh refinement. Figure 3 shows the geometrical shape of the computational domain and streamlines computed by the current method.

Figures 4 and 5 present the distributions of the streamwise velocity at different stations and centerline velocity, respectively. It can be found that the calculation yields good agreement with the measurements given by Ahmed *et al.* [6]. It is well known that most turbulence models cannot scale well in and around the recirculation zone. Therefore, the agreement between the current numerical results and experimental data is satisfactory. As shown in Reference [15], another case for the same geometry at $Re = 15\,000$ has been calculated in comparison with the experimental data and computational data given by other researchers.

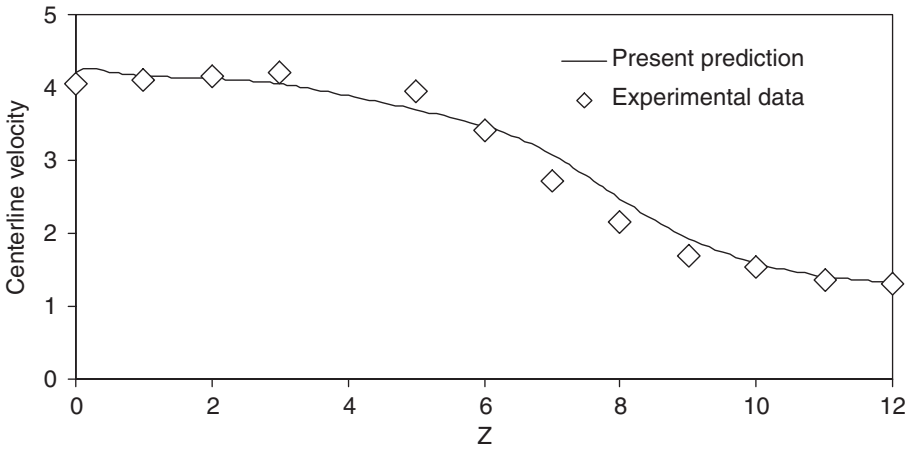

Figure 5. Distribution of the centreline velocity through the constriction (the experimental data originated from Ahmed *et al.* [6]).

These two cases illustrate that the current numerical solver is capable of simulating turbulent flows in the stenosed tube for both relatively low and high Reynolds numbers, which are usually characterized by large recirculating vortex, with good accuracy.

4.2. Oscillating turbulent flow in a straight pipe

The problems of periodic turbulent pipe flow have been studied by many researchers experimentally as well as computationally for the decades [24, 25]. As pointed out by Carpinlioglu *et al.* [26], however, the mechanism involved in turbulence generation in pulsatile pipe flows has not been recognized clearly so far. This case is computed here to test the ability of current method to simulate the unsteady turbulent flow. The calculation bases on a pipe length of 50 radii and a 161×31 grid. At the entrance, an oscillating velocity profile, which is time dependent and uniform over the cross-section, is imposed as follows:

$$U_{\text{in}}(t) = |u_m| \sin(\omega t) \tag{16}$$

The dimensionless Valensi number and Reynolds number are defined, respectively, as

$$Va = \frac{\omega r^2}{v}, \quad Re = \frac{2u_m r}{v} \tag{17}$$

where r is the radius of the pipe. The Reynolds number and Valensi number used here is 19 300 and 272, respectively. The case with the same Va and Re number has also been studied numerically by Ahn and Ibrahim [25]. As shown in References [24, 25], the critical Reynolds number for a oscillating pipe flow can be obtained by

$$\frac{Re_{\text{c}}}{\sqrt{Va}} = 882 \tag{18}$$

It can be seen that the current Reynolds number is only a bit higher than the critical Reynolds number given by Equation (18) for the Valensi number 272. The experiment data indicate

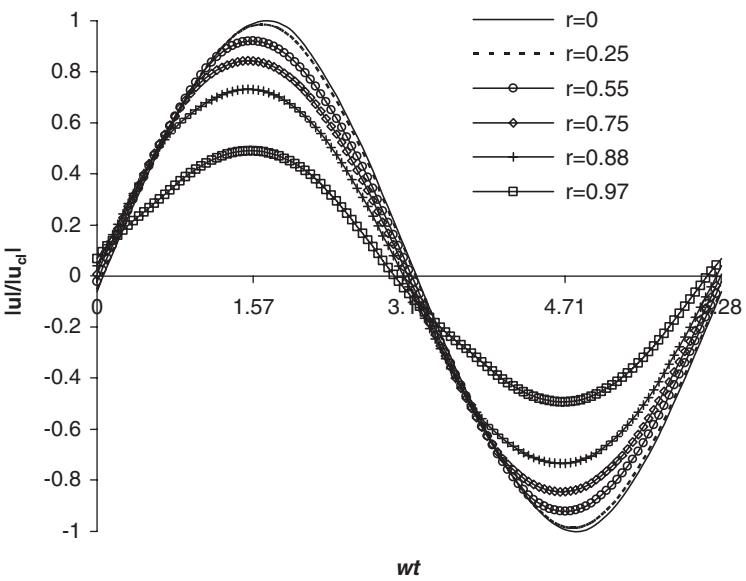

Figure 6. Turbulent axial velocity distribution versus crank angle during a cycle.

that the flow regime is in between laminar and turbulent flow (transitional regime) [25]. In this case, the number of time steps per cycle is taken to be 200.

The instantaneous velocity computed in this case versus ωt at different radial locations is shown in Figure 6. The profiles of the velocity amplitude normalized by the centerline value and the phase differences between the velocity at any radial position and that of the centreline versus the radial distance are compared with the experimental data given by Ohmi and Iguchi [24] in Figure 7. It can be found from Figure 6 that velocity amplitude increases with the distance from wall increasing. Also the phase difference between the velocity near the wall and that near the pipe centerline increases with the distance. This behaviour can be seen more clearly from Figure 7. As shown in Figure 7, the present results for both velocity amplitude and phase differences have a reasonable agreement with experimental data. Actually the phase difference profiles produced by the present method fit the experimental data of Ohmi and Iguchi [24] better than those presented by Ahn and Ibrahim [25] (their Figure 5(a)). In this case, therefore, the current numerical method succeeded in predicting the pulsatile turbulent flow in a transitional flow range within an allowable error.

5. RESULTS AND DISCUSSION

In the present study, the physiological pulsatile turbulent flows through double bell-shape stenosis are investigated in detail. The geometry of the stenosis is specified by Equation (8). As mentioned in the previous studies for a single stenosis in Reference [11], a 201×41 grid, which was highly stretched in the radial direction, was used in the cases with single stenosis and gave sufficient resolution as verified by mesh refinement. Here, the grid number

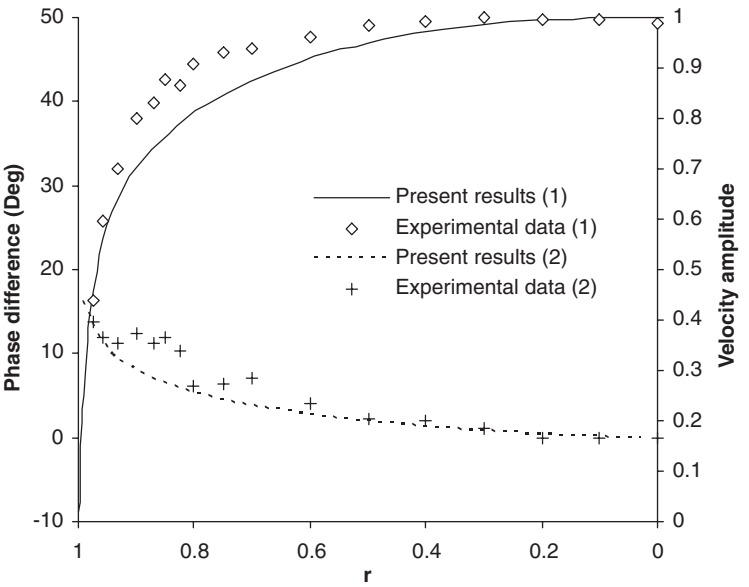

Figure 7. Profile of the velocity amplitude and phase difference versus radius (velocity amplitude—solid line: present numerical data; ⋄: experimental data by Ohmi and Iguchi [24]. Phase difference—dashed line: present numerical data; +: experimental data by Ohmi and Iguchi [24]).

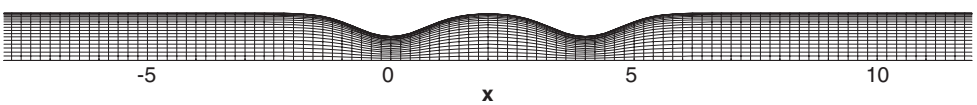

Figure 8. The (crude) computational grid in the stenosed region.

is increased according to the distance between the double stenoses so as to ensure almost the same grid density in z direction as that for the cases with single stenosis. To decide the near-wall grid sizes, a fully developed steady turbulent pipe flow at the Reynolds number 4000 has firstly been computed with a grid in which the two points at cell centers closest to the wall lie below $y^+ = 1$. Then the same grid distribution in r direction is chosen in the present pulsatile cases to ensure the enough grid refinement near the wall. The (crude) computational grid in the stenosed region is shown in Figure 8. The number of time steps per cycle is taken to be 200, which corresponds to a non-dimensional real-time step $\Delta t = 2\pi/200$.

In order to have a relatively thorough understanding of the physiological pulsatile flow through the double stenoses, the effects that the Reynolds number, the Womersley number, the constriction ratio and spacing ratio of stenoses on the flow fields are considered here. For all cases in this study, the flow characteristics are usually presented at the selected instants. The selected instants are shown in Figure 2 because these points include the key ones of the physiological velocity profiles. The selected instants are 0, $0.165T$, $0.32T$, $0.415T$, $0.6T$, $0.8T$, $0.9T$. At the instants 0, $0.32T$, $0.6T$ and $0.9T$, the net flow rates are zero or near zero. The flow

rate reaches its positive peak value at the instant $0.165T$ and reaches its negative peak value at the instant $0.415T$. The non-dimensional positive peak value is 1 and the negative peak value is just 0.252 that is only about one-fourth of the positive peak value.

5.1. Flow development in whole pulsating cycle

In this study, the physiological pulsatile flow at the Reynolds number 2000, Womersley number 30, constriction ratio 0.5 and spacing ratio 2 is considered as a basic case. The instantaneous streamline contours over a cycle under these conditions are presented in Figure 9 at the selected instants. The developments of the physiological pulsatile flow through double stenoses are discussed here.

Figure 9 shows that there is always a vortex to occur between the double stenoses at most instants except $t = 0.08T$ that is in the acceleration period. The size of the vortex between the double stenoses changes with time in a similar way to that of the vortex behind the second stenosis. Therefore, the vortex development in the downstream of the double stenoses is observed here. At the start of flow acceleration period, the flow looks like an attached flow as shown in Figure 9(b) at $t = 0.08T$. A weak recirculating vortex forms distal to the second stenosis at $t = 0.165T$ when the flow rate reaches its positive peak point as shown in Figure 9(c). After the peak flow rate point, the flow begins to decelerate. However, the recirculating vortex becomes stronger and the core of the vortex moves towards the downstream of the stenoses until $t = 0.32T$. After passing through the first zero flow rate point $t = 0.32T$, the inlet flow velocity becomes negative and vortex core position migrates towards the centreline as shown in Figure 9(f), 9(g). The vortex core continues to move downstream at $t = 0.5T$. At the time level $t = 0.6T$ when the flow rate is nearly zero, a recirculation zone occurs proximal to the first stenosis as well as distal to the second stenosis as shown in Figure 9(h). At this instant, the vortex distal to the stenosis becomes weaker and has migrated back towards the wall. Since then, the flow rate becomes very small although the flow direction changes with time. Therefore, the vortices proximal and distal to the stenoses tends to decay as seen from Figure 9(i) and (j) at $t = 0.8T$ and $0.9T$, respectively. At the end of the cycle, i.e. $t = 0$ or T, the net inlet flow becomes zero again. The recirculation zones occupy both distal and proximal region to the stenoses and the large recirculation zones fill most of flow field.

5.2. The effect of the Reynolds number

The effect of the Reynolds number on the physiological pulsatile flow through double stenoses is discussed in this work. Figures 10 and 11 show the details of the flow fields at $Re = 1000$ and 4000, respectively. The other parameters keep constant with $Wo = 30$, $c_2 = 0.5$ and $s/D = 2$. Referring to Figures 9–11, we can find that with the Reynolds number increasing, the flow fields become more complicated. For the Reynolds number 4000, more vortices are generated in flow fields at $t = 0$, 0.6 and 0.9 when the flow rates approach zero in comparison with those for the Reynolds numbers 1000 and 2000.

The mean streamline contours through the double stenoses for $Re = 1000$, 2000 and 4000 are presented in Figure 12(a)–(c), respectively. There is always a vortex to occur between the double stenoses and another vortex to occur distal to the second stenosis for the three Reynolds numbers. Both the vortex between the double stenoses and the vortex behind the second stenosis have decreasing sizes with the Reynolds number increasing. This should be

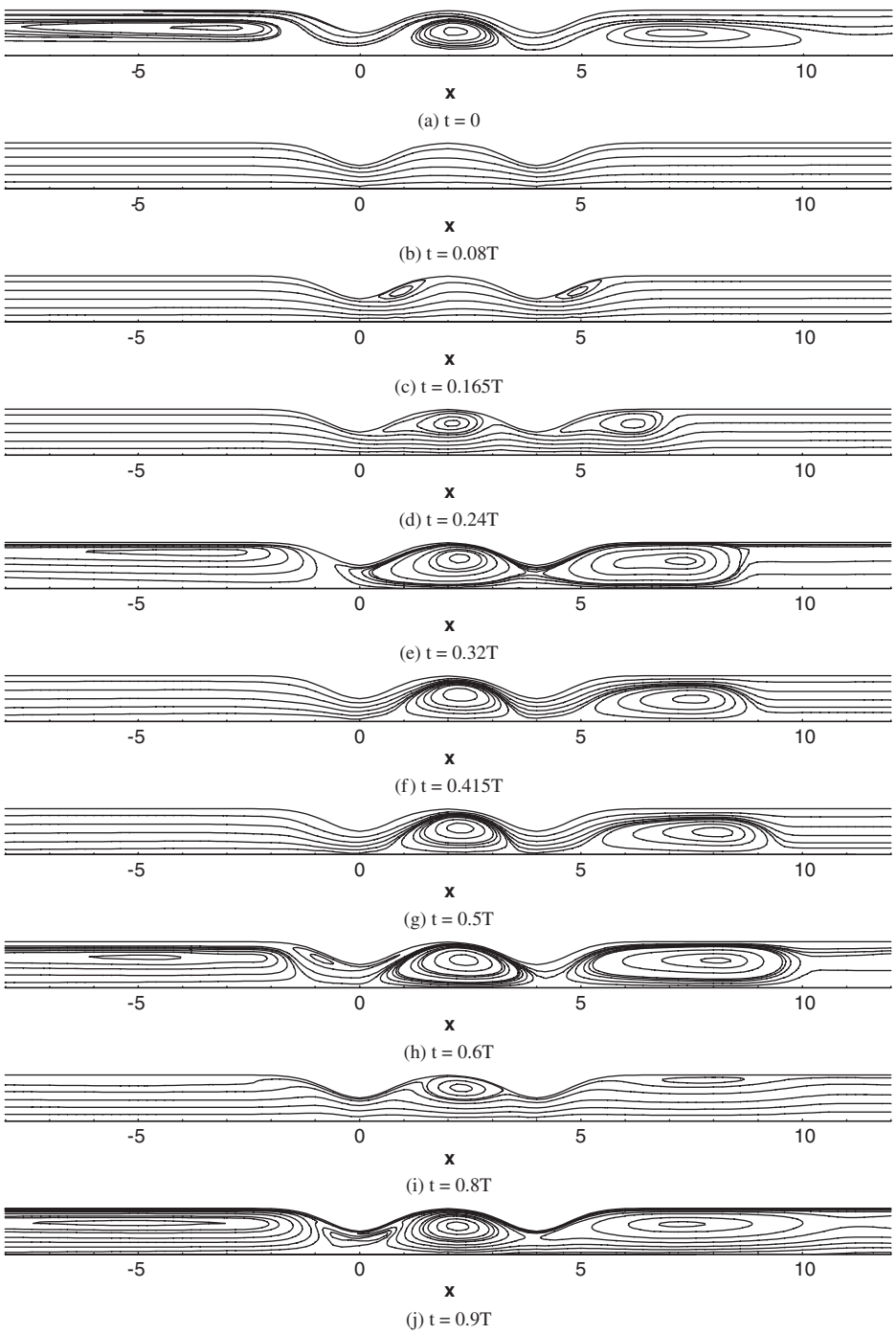

Figure 9. The streamlines of turbulent flows in the tube with double stenoses for the physiological pulsatile flow at $Re = 2000$, $Wo = 30$, $c_2 = 0.5$ and $s/D = 2$.

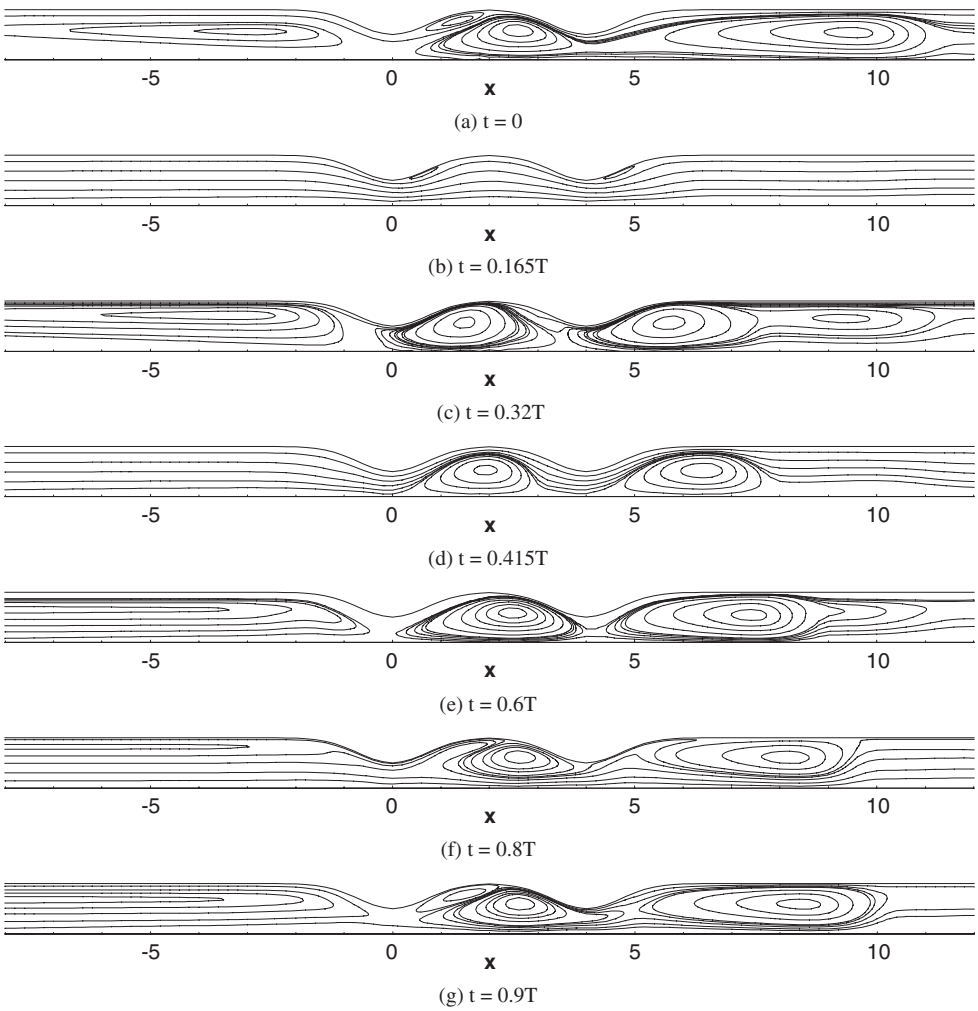

Figure 10. The streamlines of turbulent flows in the tube with double stenoses for the physiological pulsatile flow at $Re = 1000$, $Wo = 30$, $c_2 = 0.5$ and $s/D = 2$.

due to that the higher Reynolds number may lead to the stronger turbulence in the flow field which can suppress the development of separation zones near the stenosis.

The instantaneous wall vorticity and disturbance intensity distributions at the peak forward flow rate are presented in Figure 13 for double stenoses at $Re = 1000$, 2000 and 4000. The disturbance intensity is calculated by $\sqrt{2k}$ in which k denotes the non-dimensional turbulence kinetic energy. Therefore, the disturbance intensity can be referred to as an indicator of turbulence intensity. Figure 13(a) shows that there are two peak values in wall vorticity distribution both of which occur slightly upstream of the two throats, respectively. It can be seen that the both peak values go up monotonically with the Reynolds number increasing. Furthermore, the downstream peak value is a bit higher than the upstream peak value for

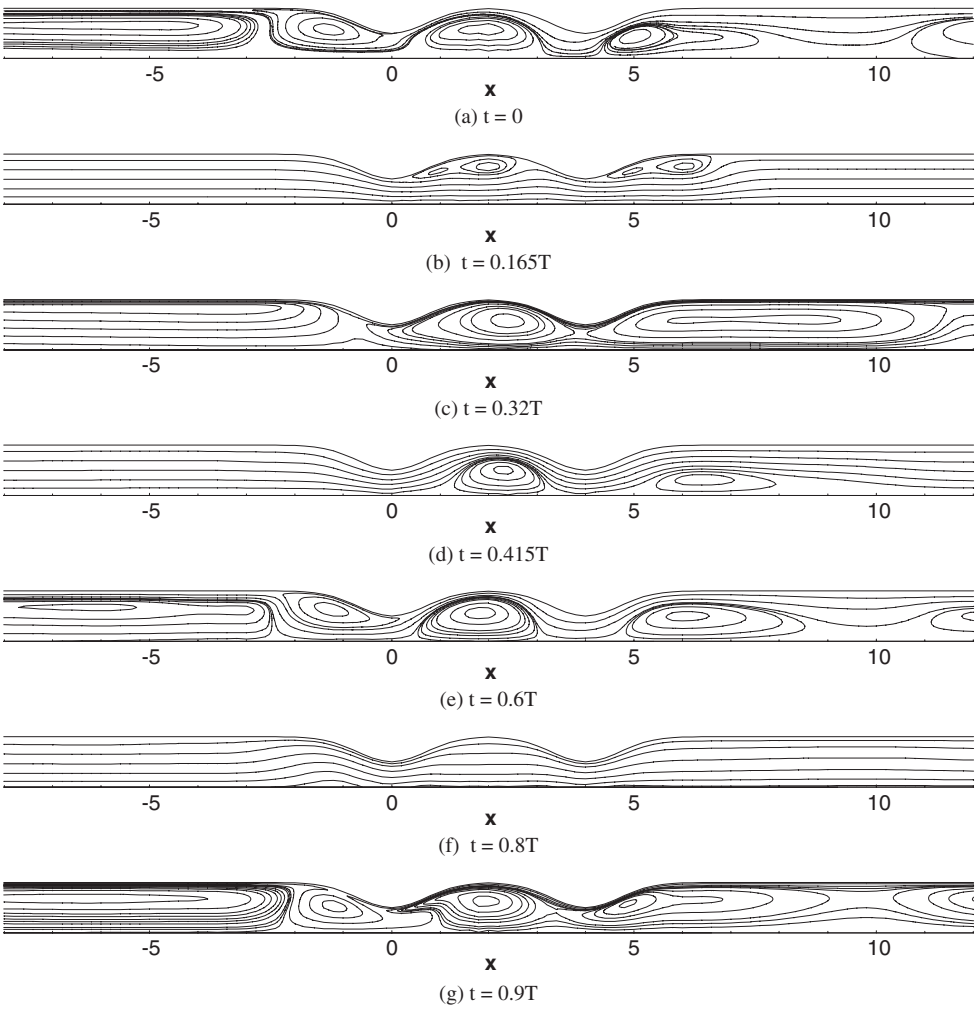

Figure 11. The streamlines of turbulent flows in the tube with double stenoses for the physiological pulsatile flow at $Re = 4000$, $Wo = 30$, $c_2 = 0.5$ and $s/D = 2$.

each Reynolds number. From Figure 13(b), it can be seen that the series stenoses produce great disturbance in the pulsatile flow fields. The flow upstream of the first stenosis has low centreline disturbance intensity. After passing through the stenoses, the disturbance intensity goes up rapidly. The disturbance intensity distribution for each Reynolds number has more than one peak point. The maximum peak value of disturbance intensity evidently grows up with the Reynolds number increasing.

The time-averaged wall vorticity distributions in one cycle for $Re = 1000$, 2000 and 4000 are displayed in Figure 14. Figure 14 shows that the both peak values of mean wall vorticity also increase with Reynolds number increasing. Different from the situation for the instantaneous wall vorticity distribution shown in Figure 13(a), the second peak value of the

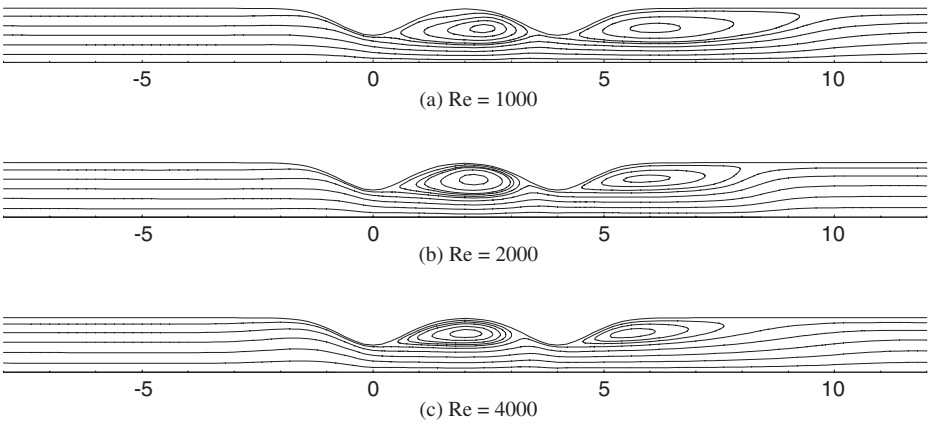

Figure 12. Mean streamlines by averaging in time over one cycle for different Reynolds numbers with double stenoses.

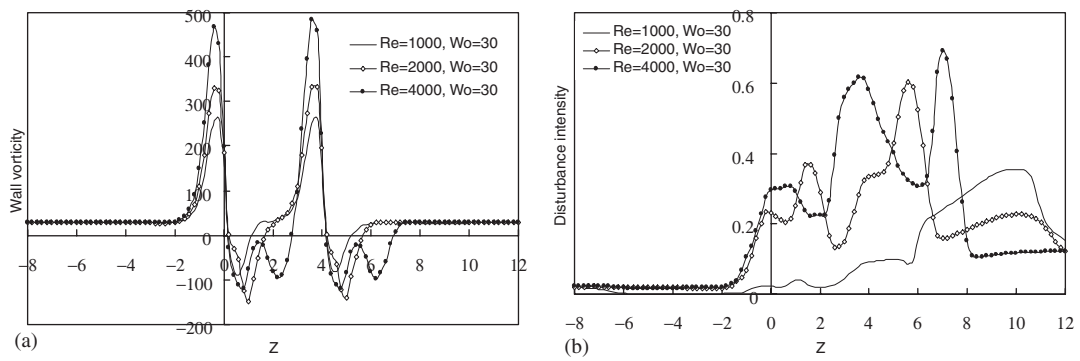

Figure 13. The distributions of the instantaneous flow parameters at the peak forward flow rate for different Reynolds numbers with double stenoses. (a) Wall vorticity; (b) centerline disturbance intensity.

mean wall vorticity is less than the first peak value for each Reynolds number. This situation is similar to that for the steady turbulent flow through the double stenoses discussed in Reference [15].

According to the analysis above, the higher Reynolds number can lead to more complicated flow field. The peak wall vorticity and centerline disturbance intensity in the flow field evidently grows up with the Reynolds number increasing. The Reynolds number has analogous influences on the time-averaged flow characteristics for the physiological pulsatile flow with those for steady turbulent flows which were shown in Reference [15].

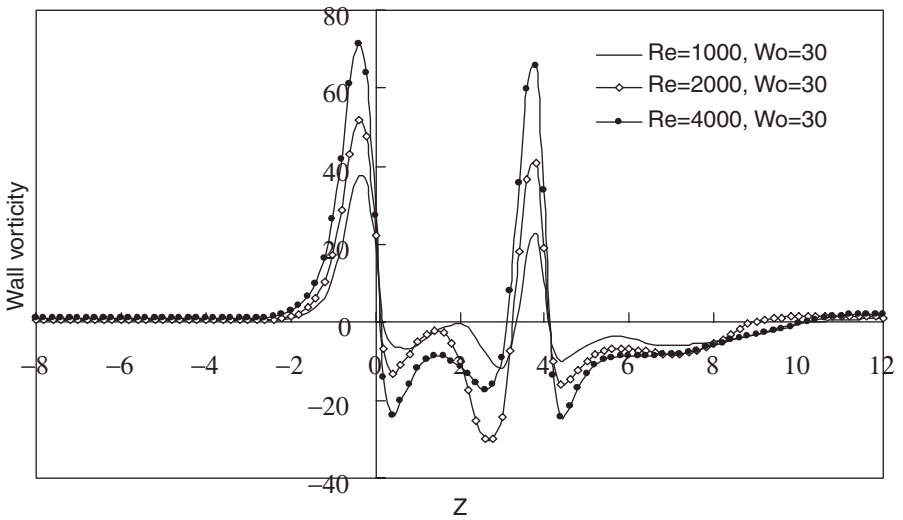

Figure 14. The time-average wall vorticity distribution in one cycle for different Reynolds numbers with double stenoses.

5.3. The effect of the Womersley number

The details of flow fields for $Wo = 10$ and $Wo = 50$ with $Re = 2000$, $c_2 = 0.5$ and $s/D = 2$ are also presented here to examine the effect of the Womersley number. The streamline contours for the above Womersley numbers are shown in Figures 15 and 16, respectively. For $Wo = 10$, it can be seen that corresponding to the non-zero instantaneous flow rate, there is always a recirculating vortex to form in the downstream of stenoses along the flow rate direction. For $Wo = 30$ and 50, the recirculation zone almost always occurs on the right side of stenosis except at the instants when the flow rate is zero or near zero. This is because for the high Womersley numbers, the flow fields are strongly influenced by the flow rates at the previous time levels. For the physiological flow, the forward flow rate is much higher than the backward flow rate and therefore usually predominates in the periodic development of the flow field. Besides, the recirculation zones always prefer to simultaneously occur both proximal and distal to the stenosis at the instants 0, $0.32T$, $0.6T$ and $0.9T$ when the net flow rate approaches zero for each Womersley number.

The instantaneous wall vorticity and disturbance intensity distributions at the peak forward flow rate are presented in Figure 17 for the Womersley numbers 10, 30 and 50. Figure 17(a) shows that the first peak value of instantaneous wall vorticity at this instant is not significantly affected by the variation of the Womersley number while the second peak value grows up to some extent with the Womersley number increasing. It can be found that the wall vorticity for $Wo = 30$ and 50 can recover more rapidly to the upstream level than that for $Wo = 10$ after passing through the stenoses. Figure 17(b) indicates that the disturbance intensity distribution has more than one peak points and the maximum peak points are all located downstream of the second stenosis for the three Womersley numbers. The maximum peak value of centerline disturbance intensity reduce with the Womersley number increasing,

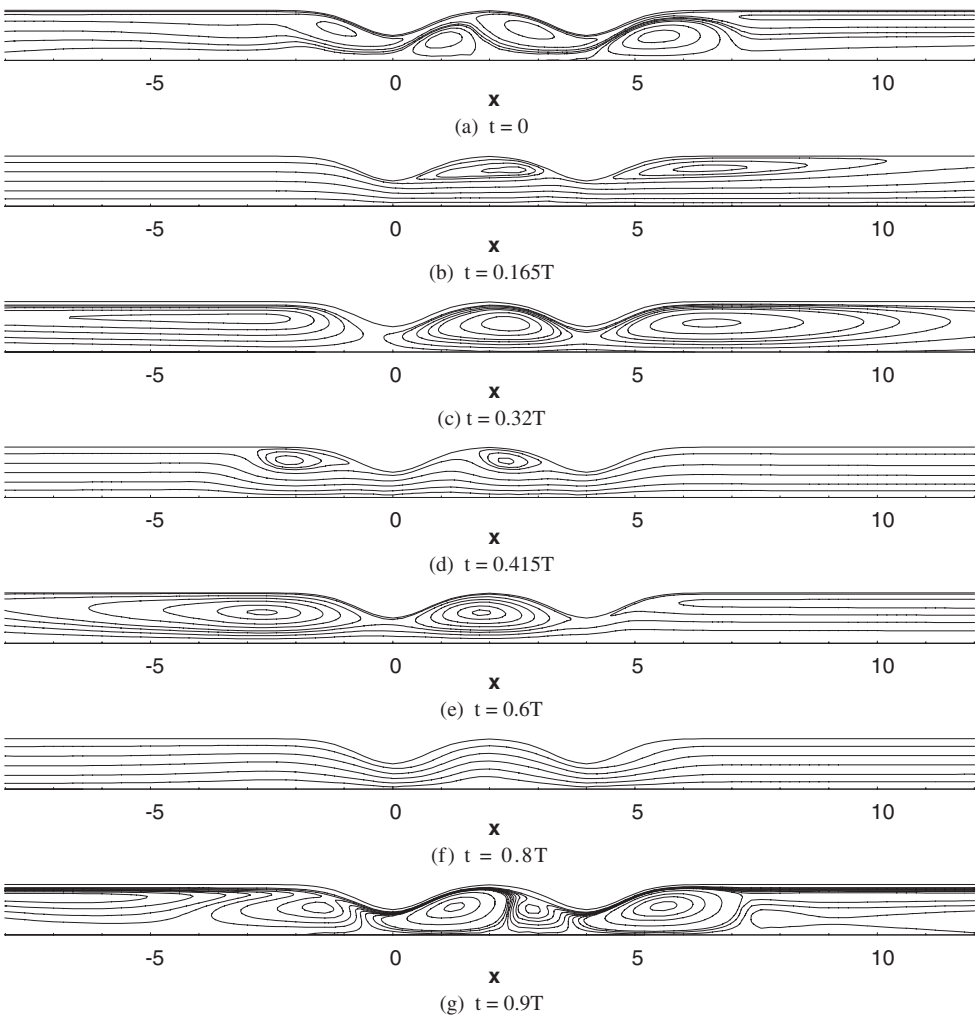

Figure 15. The streamlines of turbulent flows in the tube with double stenoses for the physiological pulsatile flow at $Re = 2000$, $Wo = 10$, $c_2 = 0.5$ and $s/D = 2$.

which illustrates that the turbulence intensity decreases with the Womersley number increasing for the same Reynolds number. This observation is consistent with the situation for the oscillating flow in a straight circular pipe [25, 26]. It can be inferred that for a higher Womersley number, the generated disturbance does not have enough time to fully grow up and soon is suppressed by the next acceleration phase in which the favourite pressure gradient becomes strong.

The time-averaged wall vorticity distributions over one cycle for $Wo = 10$, 30 and 50 are shown in Figure 18. From this figure, it can be seen that the second peak values in the mean wall vorticity distributions are almost the same for the three Womersley numbers while the first peak value for $Wo = 50$ is a bit lower than those for $Wo = 10$ and 30. In total, the peak values

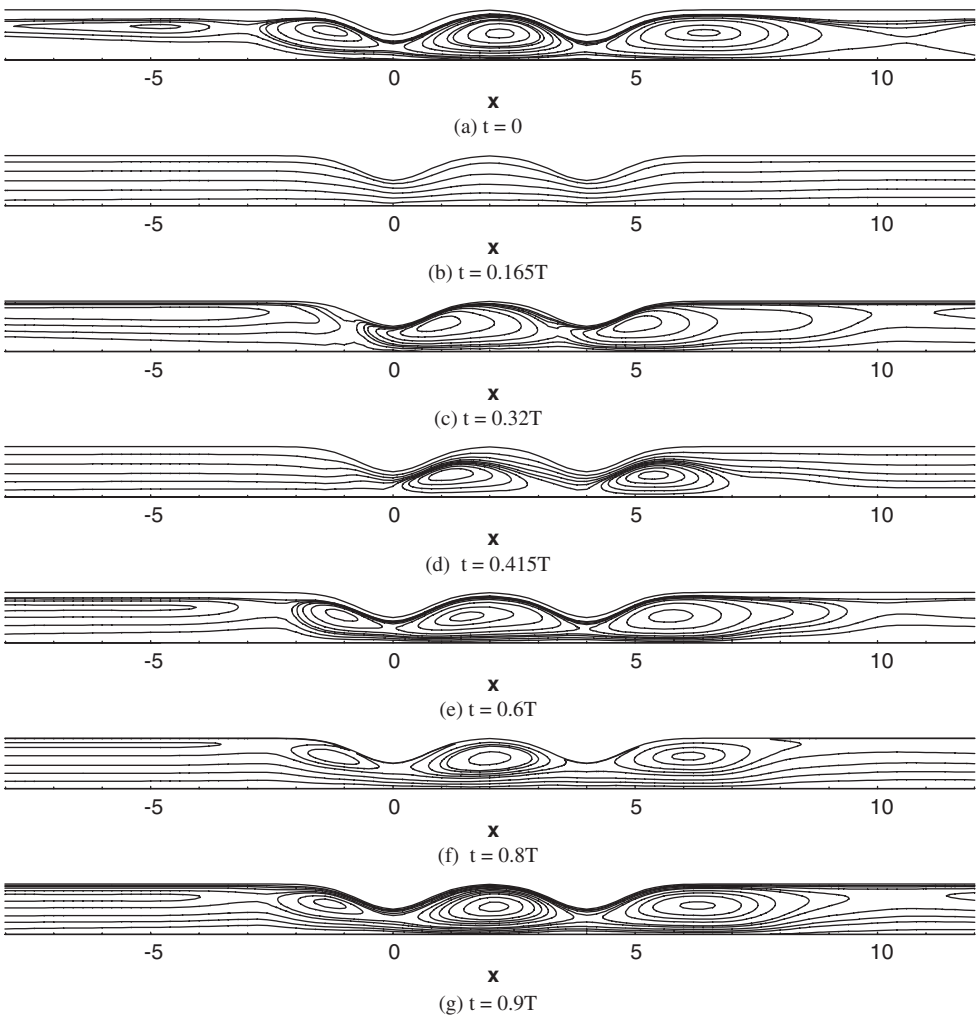

Figure 16. The streamlines of turbulent flows in the tube with double stenoses for the physiological pulsatile flow at $Re = 2000$, $Wo = 50$, $c_2 = 0.5$ and $s/D = 2$.

of mean wall vorticity are not greatly influenced by the variation of the Womersley number, which is in agreement with the situation for the instantaneous wall vorticity distribution at $t = 0.165$ as discussed above. Figure 18 shows that for the Womersley numbers 10 and 30, the downstream peak value is evidently lower than the upstream peak value in the mean wall vorticity distribution.

5.4. The effect of the constriction ratio of stenoses

In order to consider the effect of the constriction ratio of stenosis, the constriction ratio of the upstream stenosis in a tube is fixed at 0.5 while the downstream stenosis is allowed to vary.

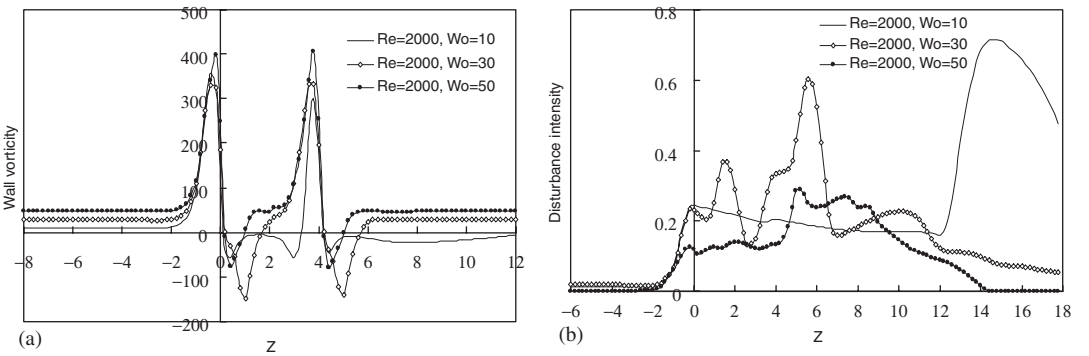

Figure 17. The distributions of the instantaneous flow parameters at the peak forward flow rate for different Womersley numbers with double stenoses. (a) Wall vorticity; (b) centerline disturbance intensity.

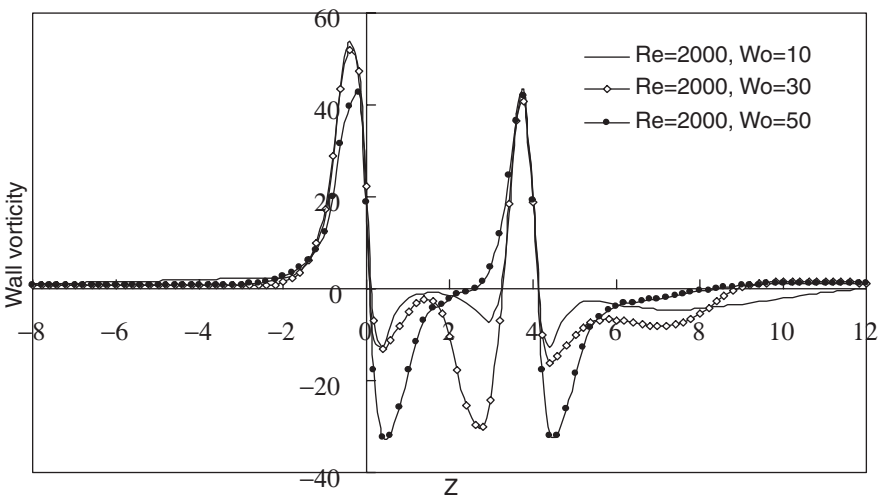

Figure 18. The time-average wall vorticity distribution in one cycle for different Womersley numbers with double stenoses.

The numerical results are compared for the constriction ratios of the downstream stenosis $c_2 = 0.2$, 0.5 and 0.6 with the same Re and Wo. The streamline contours in one cycle for $c_2 = 0.2$ and 0.6 with $Re = 2000$ and $Wo = 30$ are presented in Figures 19 and 20, respectively. Actually, from Figure 19, it can be noticed that the vortex distribution in the flow fields for $c_2 = 0.2$ are very similar to that for single-stenosis case (shown in Reference [11]). Evidently, the second stenosis with $c_2 = 0.2$ has such small constriction ratio that it have not put great impact on the flow field development. Referring to Figures 9, 19 and 20, it can be found that with the second constriction ratio increasing, the flow fields become more complicated. There are more vortices to be generated in the flow fields for $c_2 = 0.5$, 0.6 than those for $c_2 = 0.2$.

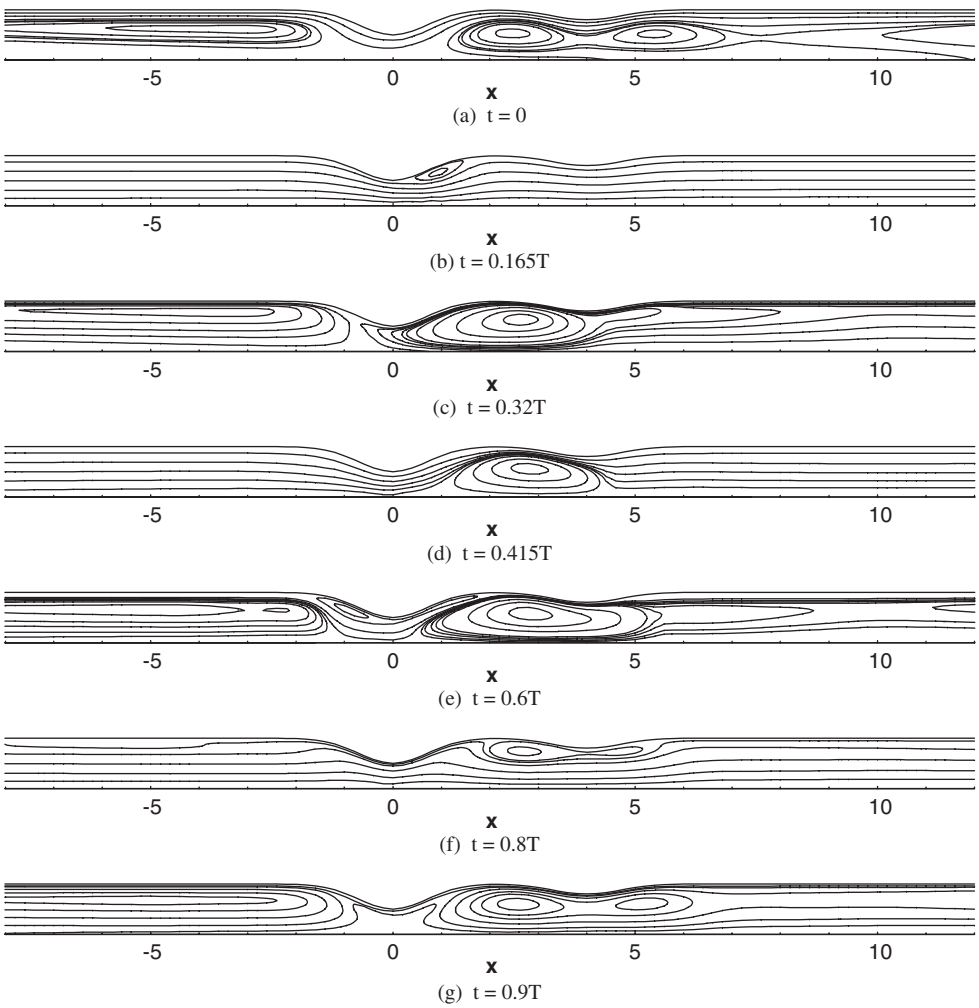

Figure 19. The streamlines of turbulent flows in the tube with double stenoses for the physiological pulsatile flow at $Re = 2000$, $Wo = 30$, $c_2 = 0.2$ and $s/D = 2$.

The vortex distribution in the flow fields for $c_2 = 0.6$ is very similar to that for $c_2 = 0.5$. But the vortices downstream of the second stenosis for $c_2 = 0.6$ are stronger than the corresponding vortices for $c_2 = 0.5$.

The mean streamline contours for the $c_2 = 0.2$, 0.5 and 0.6 are shown in Figure 21(a), (b) and (c), respectively. Figure 21 shows that there is a vortex to occur between the double stenoses for the three constriction ratios. There is another vortex to occur distal to the second stenosis for $c_2 = 0.5$ and 0.6 while it is not case for $c_2 = 0.2$ because of too small constriction ratio. It can be found that the vortex distal to the second stenosis has increasing size with the constriction ratio increasing.

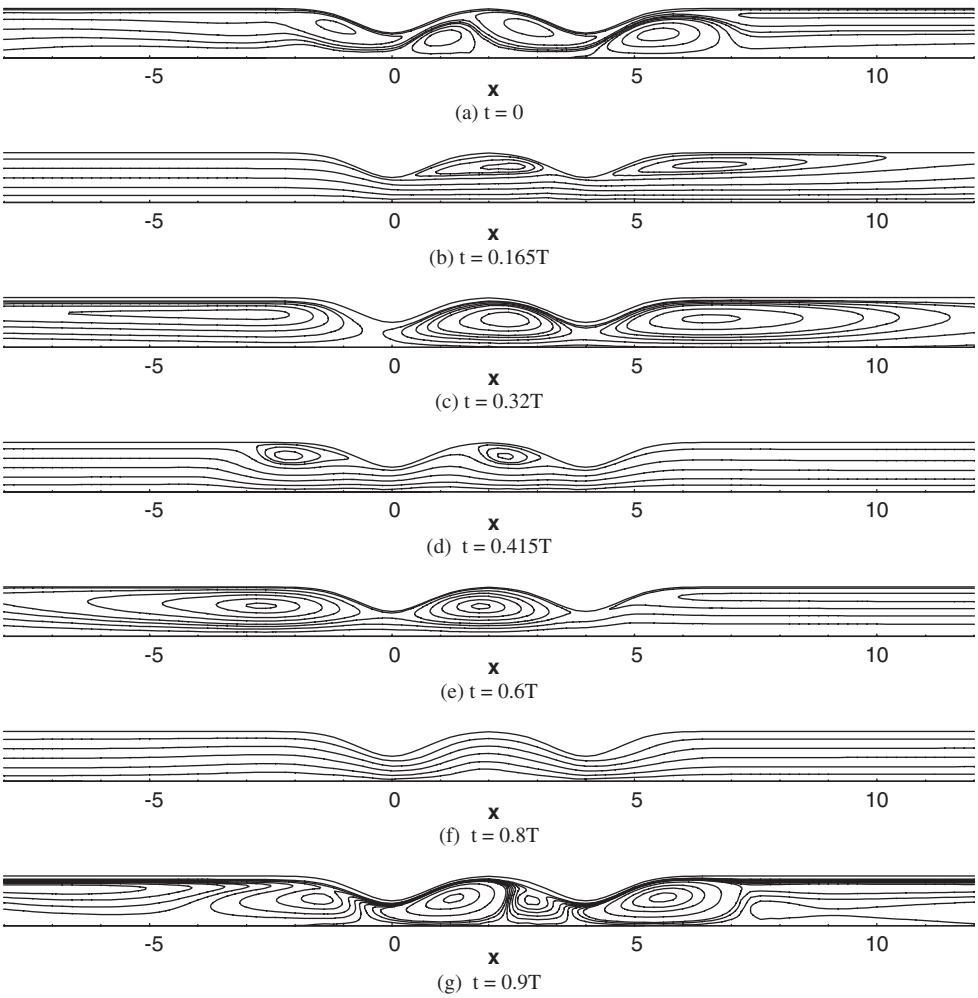

Figure 20. The streamlines of turbulent flows in the tube with double stenoses for the physiological pulsatile flow at $Re = 2000$, $Wo = 30$, $c_2 = 0.6$ and $s/D = 2$.

The instantaneous wall vorticity, wall pressure, centreline velocity and disturbance intensity distributions at the peak forward flow rate are shown in Figure 22 for $c_2 = 0.2$, 0.5 and 0.6. It can be found that the upstream peak values of the distributions of these flow variables for all the three constriction ratios are almost fully the same, which mean that the downstream stenosis does not make perceptible contributions to the upstream flow fields. At the same time, the downstream peak values of these instantaneous variables all grow up dramatically with the constriction ratio c_2 increasing. Figure 22(a) shows that the downstream peak wall vorticity for $c_2 = 0.6$ is so high that its value is more than twice as high as that for $c_2 = 0.5$ although the area reduction caused by the second stenosis increases only from 75 to 84% when $c_2 = 0.5$ and 0.6. From Figure 22(b) and (c), it can be seen that the wall pressure

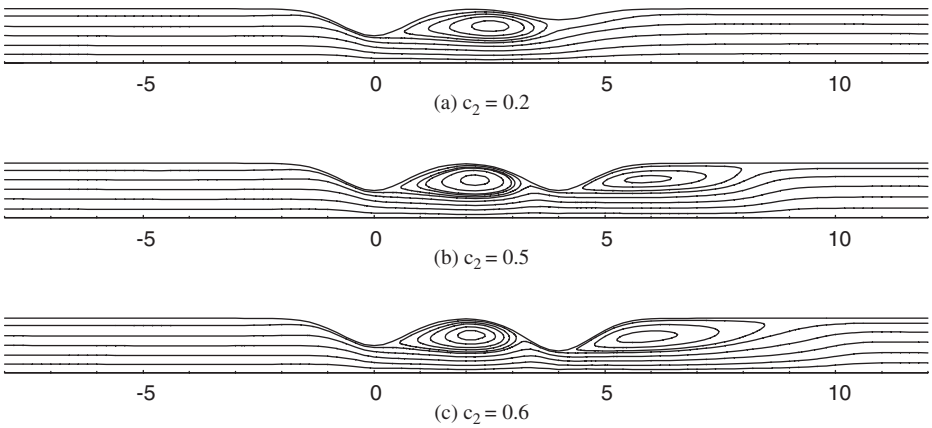

Figure 21. Mean streamlines by averaging in time over one cycle for different constriction ratios.

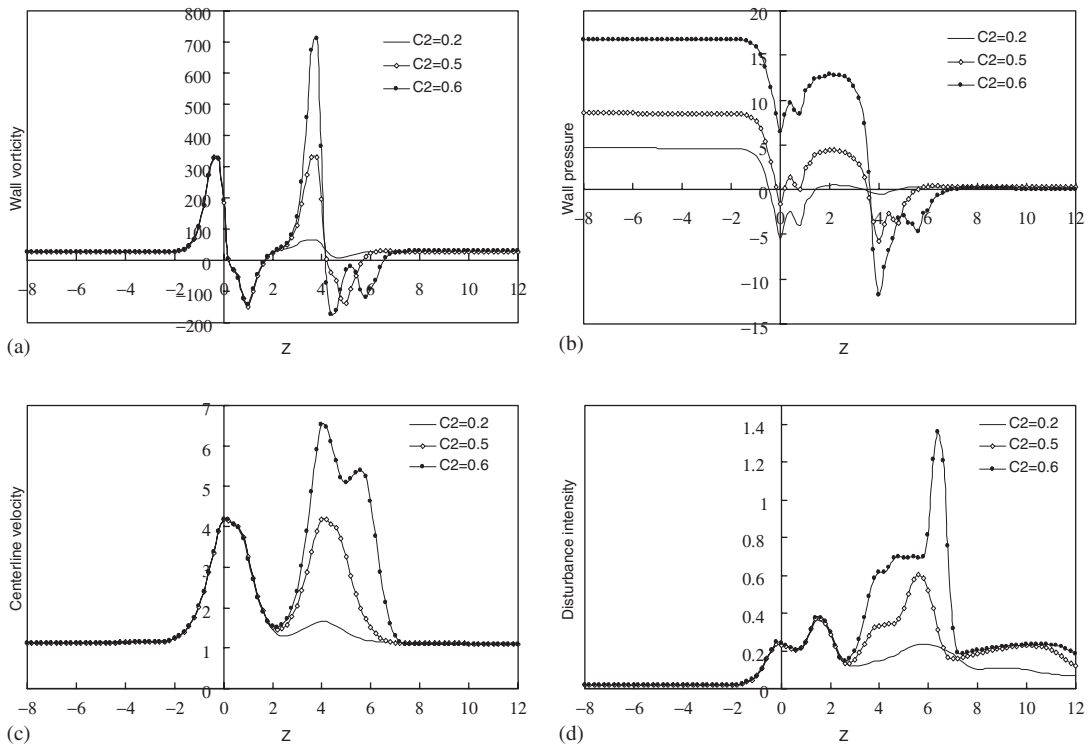

Figure 22. The distributions of the instantaneous flow parameters at the peak forward flow rate for different constriction ratios with double stenoses.

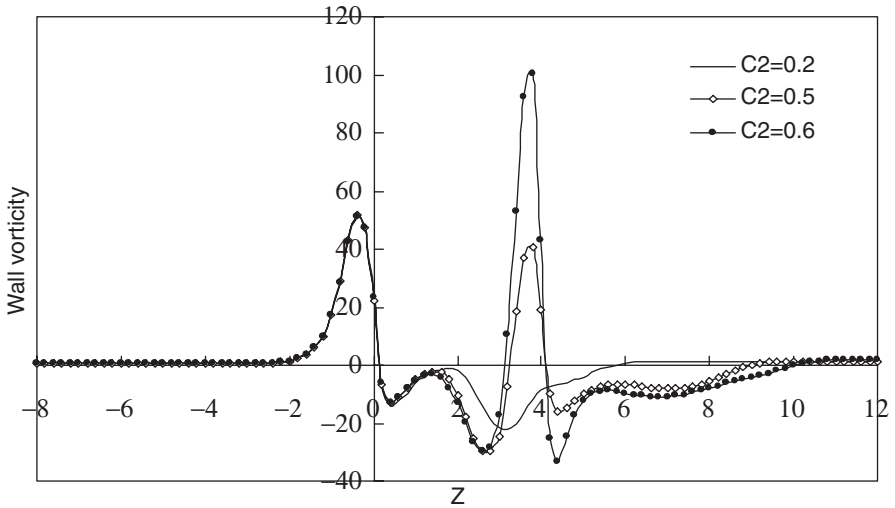

Figure 23. The time-average wall vorticity distribution in one cycle for the different constriction ratios with double stenoses.

drop and peak centreline velocity caused by the second stenosis increase rapidly with the constriction ratio c_2 increasing. Therefore, the severe stenosis may cause the pressure loss to increase dramatically. Figure 22(d) shows that the severe constriction ratio leads to a dramatic increase of the turbulence intensity in the flow field. It is surprising that the variation range of peak disturbance intensity caused by the stenosis with $c_2 = 0.6$ is more than six times and two times as high as those by the stenoses with $c_2 = 2$ and 0.5, respectively.

The time-averaged wall vorticity distributions over one cycle for $c_2 = 0.2$, 0.5 and 0.6 are presented in Figure 23. The distributions of mean wall vorticity before the second stenosis are fully the same for the three cases $c_2 = 0.2$, 0.5 and 0.6. At the same time, the increase of the constriction ratio c_2 causes the downstream peak mean wall vorticity to rapidly grow up. This observation is consistent with that for the distribution of the instantaneous wall vorticity at the peak forward flow rate.

5.5. The effect of the stenosis spacing ratio

The behaviours of the physiological pulsatile flow through double stenoses are investigated with stenosis spacing ratios from 2 to ∞ at $Re = 2000$ and $Wo = 30$. The constriction ratio of the second stenosis is also set to 0.5 as well as that of the first stenosis. The mean streamline contours through the double stenoses for s/D from 2 to ∞ are presented in Figure 24. It can be seen that the recirculation zone fills part of the valley region between the two stenoses for $s/D = 2$ and 3. When s/D is 4, 5 and ∞, the vortices between the double stenoses keep constant and have almost the same size because the valley region is enough large and has less limitation to the formation of vortex. The size of the recirculation zone distal to the second stenosis decreases with s/D increasing until s/D reaches 4. For $s/D = 5$, the size of the corresponding recirculation zone becomes slightly larger than that for $s/D = 4$ and is still less than that for $s/D = 2$. Figure 24 shows that the vortex behind the second

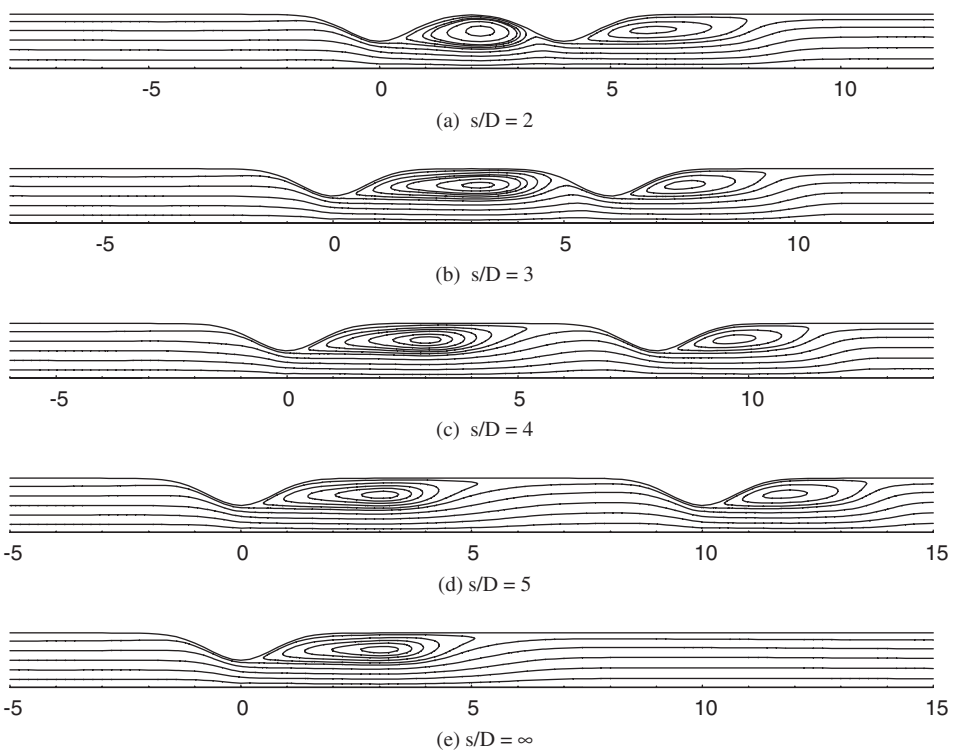

Figure 24. Mean streamlines by averaging in time over one cycle for different spacing ratios with double stenoses.

stenosis in the double-stesnosis case is usually smaller than the corresponding vortex in the single-stenosis case ($s/D = \infty$). As mentioned before, the forward flow rate predominates for the physiological pulsatile flow. Therefore, the double stenoses can cause the higher turbulence intensity which lead to the smaller vortex in the downstream of the stenoses than the single stenosis.

The instantaneous wall vorticity and disturbance intensity distributions at peak forward flow rate are presented in Figure 25 for the spacing ratios $s/D = 2$, 3, 4 and 5. It can be found again that the distributions of instantaneous wall vorticity and disturbance intensity in the vicinity of the upstream stenosis are almost the same for all the spacing ratios. This illustrates that the downstream stenosis do not have any evident influences on the upstream flow fields for different spacing ratios. Figure 25(a) shows that the downstream peak value of wall vorticity increases with spacing ratio increasing until the spacing ratio s/D reaches 4 and after that, the downstream peak value begins to reduce. The distribution of the centerline disturbance intensity has the same trends as that of the wall vorticity, as shown in Figure 25(b). It is demonstrated that in this work, the double stenoses have the strongest superposed effects on the flow fields when the distance between the double stenoses is $4D$. When the distance between the double stenoses is more than $4D$, the first stenosis has a weaker and weaker effect on the flow field downstream of the second stenosis with s/D increasing. The downstream peak

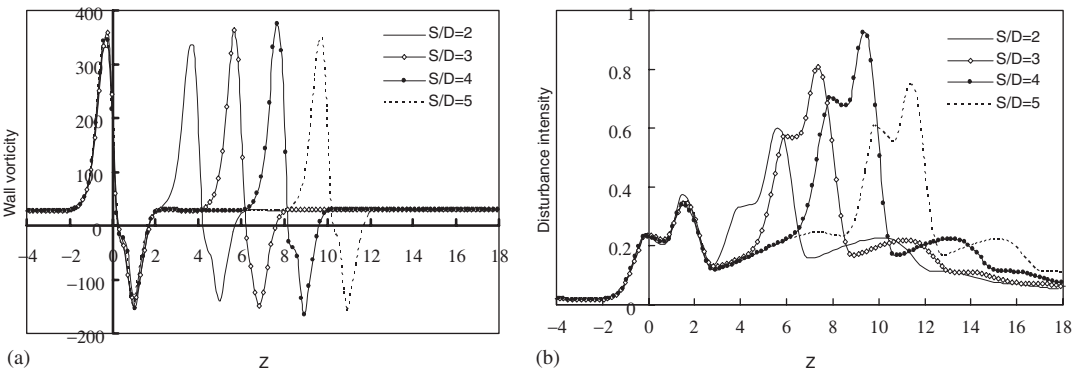

Figure 25. The distributions of the instantaneous flow parameters at the peak forward flow rate for different spacing ratios with double stenoses. (a) Wall vorticity; (b) centerline disturbance intensity.

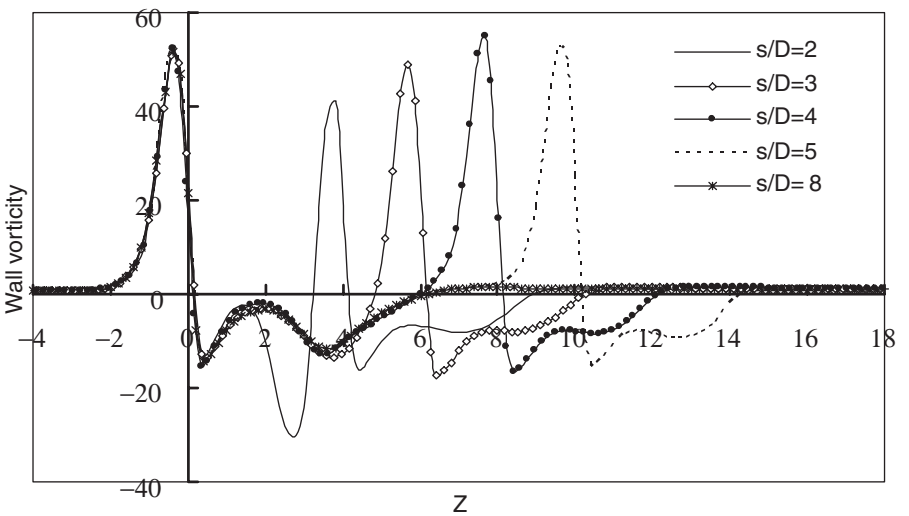

Figure 26. The time-average wall vorticity distribution in one cycle for the different spacing ratios with double stenoses.

values of centerline disturbance intensity are much higher than the corresponding upstream ones, respectively. Especially for $s/D = 4$, the downstream peak disturbance intensity reaches about 2.5 times as high as the upstream one.

The time-averaged wall vorticity distributions over one cycle for $s/D = 2$, 3, 4, 5 and ∞ are shown in Figure 26. Figure 26 shows that the mean wall vorticity distributions for different spacing ratios have the similar characteristics to the instantaneous wall vorticity distributions as shown in Figure 25(a) although the values of the former are all much less than those of the latter. From Figure 26, it can be seen that the distributions of the wall vorticity near

the first stenosis for the double-stenosis model, such as $s/D = 2$, 3, 4 and 5, are almost fully the same as that for $s/D = \infty$ that represents a single-stenosis model. This means that the downstream stenosis do not put any perceptible impact on developments of the upstream flow fields. Evidently, this is because the forward flow rate far exceeds the backward flow rate and so predominates in the periodic development of the flow field for the physiological flow.

6. CONCLUSIONS

In the present study, the flow behaviours through double stenoses for the physiological pulsatile flow are studied by considering the effects of the Reynolds number, Womersley number, constriction ratio and spacing ratio of the stenoses. Especially, the mutual influences between the double stenoses under different flow conditions are considered.

The Reynolds number can greatly influence the physiological flow fields through the double stenoses. The vortices both between the double stenoses and behind the second stenosis have decreasing sizes with the Reynolds number increasing. The peak values of the wall vorticity and centerline disturbance intensity increase rapidly with the Reynolds number increasing. Totally, the peak values of wall vorticity are not greatly influenced by the variation of the Womersley number. The peak turbulence intensity in the flow fields decreases with the Womersley number increasing for the same Reynolds number. With the constriction ratio of the downstream stenosis increasing, the flow fields become more complicated and have more recirculating vortices to form. All the downstream peak values of the flow variables considered grow up dramatically with the constriction ratio c_2 increasing. The severe constriction ratio leads to a miraculous increase of the turbulence intensity in the flow field. The behaviours of the physiological pulsatile flow are investigated with different spacing ratios between double stenoses from 2 to ∞. The double stenoses lead to the higher peak turbulence disturbance and the greater area with comparatively high turbulence intensity distal to the stenoses in comparison with the single stenosis. The downstream peak values of wall vorticity and centerline disturbance intensity increases with spacing ratio increasing until the spacing ratio s/D reaches 4 and after that, the downstream peak value begins to reduce. It is inferred that under the current flow conditions, the double stenoses have the strongest superposed effects on the flow fields when the distance between the double stenoses is $4D$. When s/D is more than 4, the first stenosis has a weaker and weaker effect on the flow field downstream of the second stenosis with s/D increasing further. Besides, with the same Reynolds number and Womersley number, the distributions of the important flow variables considered here in the vicinity of the upstream stenosis are almost the same for different constriction ratios c_2 and spacing ratios s/D, which illustrates that the downstream stenosis usually does not have perceptible influences on the upstream flow fields. This suggests that for the physiological pulsatile flow, the forward flow rate predominates in the periodic development of the flow field.

REFERENCES

1. Roach MR. Poststenotic dilatation in arteries. *Cardiovascular Fluid Dynamics* 1972; **2**:111–139.
2. Ku DN. Blood flow in arteries. *Annual Review of Fluid Mechanics* 1997; **29**:399–434.
3. Mittal R, Simmons SP, Udaykumar HS. Application of large-eddy simulation to the study of pulsatile flow in a modeled arterial stenosis. *ASME Journal of Biomechanical Engineering* 2001; **123**:325–332.

4. Clark C. Turbulent velocity measurements in a model of aortic stenosis. *Journal of Biomechanics* 1976; **9**: 677–687.
5. Deshpande MD, Giddens DP. Turbulence measurements in a constricted tube. *Journal of Fluid Mechanics* 1980; **97**:65–89.
6. Ahmed SA, Giddens DP. Velocity measurements in steady flow through axisymmetric stenoses at moderate Reynolds numbers. *Journal of Biomechanics* 1983; **16**:505–516.
7. Yongchareon W, Young DF. Initiation of turbulence in models of arterial stenoses. *Journal of Biomechanics* 1979; **12**:185–196.
8. Ahmed SA. An experimental investigation of pulsatile flow through a smooth constriction. *Experimental Thermal and Fluid Science* 1998; **17**:309–318.
9. Deshpande MD. Steady laminar and turbulent flow through vascular stenoses models. *Ph.D. Thesis*, Georgia Institute of Technology, 1977.
10. Ghalichi F, Deng X, Champlain AD, Douville Y, King M, Guidoin R. Low Reynolds number turbulence modeling of blood flow in arterial stenoses. *Biorheology* 1998; **35**:281–294.
11. Liao W, Lee TS, Low HT. Numerical study of physiological turbulent flows through stenosed arteries. *International Journal of Modern Physics C* 2003; **14**(5):635–659.
12. Lee TS. Numerical studies of fluid flow through tubes with double constrictions. *International Journal for Numerical Methods in Fluids* 1990; **11**:1113–1126.
13. Lee TS. Steady laminar fluid flow through variable constrictions in vascular tubes. *ASME Journal of Fluids Engineering* 1994; **116**:66–71.
14. Damodaran V, Rankin GW, Zhang C. Numerical study laminar flow through tubes with multiple constrictions using curvilinear co-ordinates. *International Journal for Numerical Methods in Fluids* 1996; **23**:1021–1041.
15. Lee TS, Liao W, Low HT. Numerical simulation of turbulent flow through series stenoses. *International Journal for Numerical Methods in Fluids* 2003; **42**:717–740.
16. Wilcox DC. *Turbulence Modeling for CFD.* DCW Industries, Inc. 1993 and 1998.
17. Lee TS, Liao W, Low HT. Development of an artificial compressibility methodology with implicit LU-SGS method. *International Journal of Computational Fluid Dynamics* 2001; **15**:197–208.
18. Lee TS, Liao W, Low HT. Turbulence modeling using artificial compressibility with implicit LU-SGS method. *Proceedings of the International Conference on Computational Fluid Dynamics* 2, Sydney, Australia. Springer: Berlin, 2002.
19. Chorin AJ. A numerical method for solving incompressible viscous flow problems. *Journal of Computational Physics* 1967; **2**:12–26.
20. Wood NB. Aspects of fluid dynamics applied to the larger arteries. *Journal of Theoretical Biology* 1999; **199**:137–161.
21. Roe PL. Approximate Riemann solvers, parameter, vectors, and difference schemes. *Journal of Computational Physics* 1981; **43**:357–372.
22. McDonald DA. The relation of pulsatile pressure to flow in arteries. *Journal of Physiology* 1955; **127**: 533–552.
23. Zendehbudi GR, Moayeri MS. Comparison of physiological and simple pulsatile flows through stenosed arteries. *Journal of Biomechanics* 1999; **32**:959–965.
24. Ohmi M, Iguchi M. Critical Reynolds number in an oscillating pipe flow. *Bulletin of the JSME* 1982; **25**: 165–172.
25. Ahn KH, Ibrahim MB. Laminar/turbulent oscillating flow in circular pipes. *International Journal of Heat and Fluid Flow* 1992; **13**:340–346.
26. Carpinlioglu MO, Gundogdu MY. A critical review on pulsatile pipe flow studies directing towards future research topics. *Flow Measurement and Instrumentation* 2001; **12**:163–174.

